

Generalized Input Impedance Modeling of TL-Network-Based HFDPS for Validating Frequency-Dependent Criteria for Power-Signal Integrity

Ankit Gupta ^{ID}, *Student Member, IEEE*, Nikhil Kumar, *Student Member, IEEE*, and Sudip K. Mazumder ^{ID}, *Fellow, IEEE*

Abstract—Adjusting the transmission-line (TL) length or using active compensation is pursued in high-frequency-distributed power systems (HFDPSs) as a possible remedy for addressing the TL effects. Although adjusting the TL length is primarily limited to printed-circuit-board (PCB) level implementations, active compensation yields higher expense and complexity. To mitigate TL effects under periodic condition, generalized input impedance modeling of a TL-network-based HFDPS feeding linear load(s) is provided. Using this generalized model, a frequency-dependent criterion for maintaining power-signal integrity is outlined for scenario centric single-/multiple-input single-/multiple-output HFDPS topologies. Selection of such a transmission frequency is important for designing a HFDPS to avoid deterioration of voltage and current, rupturing the TL insulation, and increased losses owing to the TL effect. Validations of the frequency-dependent criteria have been carried out using simulation and experiments in time and frequency domains.

Index Terms—Characteristic impedance, high frequency, power transfer, transmission line (TL).

I. INTRODUCTION

CONVENTIONALLY, distributed power systems (DPSs) are based on dc or low-frequency ac power delivery. Fig. 1 displays a high-frequency DPS (HFDPS), which offers a promising alternative with several flexible applications [1] [2]. A HFDPS is outlined in [3] [4] to minimize system complexity, reduce power-electronics stages, and enhance the efficiency, power density, and system dynamics. Improvements in the device technology have facilitated HFDPS by enabling HF operation at reduced losses. This has accelerated the

Manuscript received April 9, 2017; revised August 29, 2017; accepted September 18, 2017. Date of publication October 2, 2017; date of current version January 16, 2018. This work was supported by the National Science Foundation under Grant 1239118. (*Corresponding author: Sudip K. Mazumder.*)

The authors are with the Laboratory of Energy and Switching-Electronics Systems, Department of Electrical and Computer Engineering, University of Illinois at Chicago, Chicago, IL 60607 USA (e-mail: agupta70@uic.edu; nkumar22@uic.edu; mazumder@uic.edu).

Color versions of one or more of the figures in this paper are available online at <http://ieeexplore.ieee.org>.

Digital Object Identifier 10.1109/TIE.2017.2758739

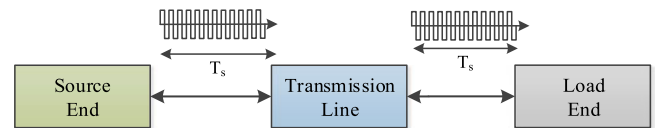


Fig. 1. Illustration of a HFDPS overview.

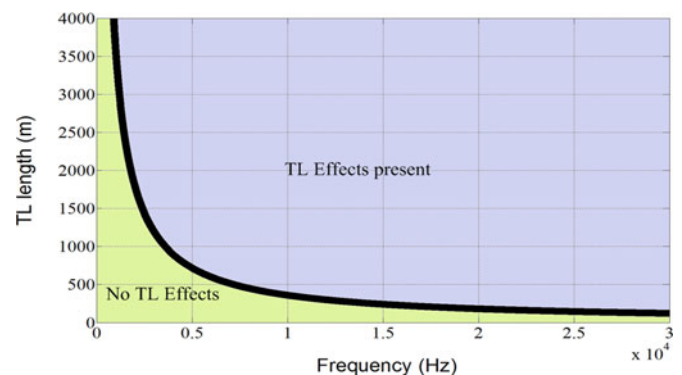


Fig. 2. Illustration of TL length at which TL effect onsets for a given frequency. The parameters of the TL are captured in Table I.

applications of the HFDPS in areas such as hybrid-electric vehicle, all-electric ships, telecommunication, computers, and digitization of electricity [1], [5]–[12].

On the basis of the span of a HFDPS and the frequency of wave transmission through a TL, HFDPS is subdivided into two categories: one that encounters transmission-line (TL) effect [13]–[22] and the other, which does not [23]–[26]. When the physical length of a TL is comparable to the length of the wave being transmitted through it, TL effect comes into play. The latter leads to loss of integrity of the power signal being transmitted through the TL [27]–[29]. The simulation result in Fig. 2 captures the variations in the length of a TL (with the parameters tabulated in Table I) at which the onset of TL effect occurs as a function of the frequency of wave transmission [27]. Fig. 2 shows that, as the frequency of the wave transmission increases, the length at which the TL effect onsets decreases. Such effects often accompany overvoltages in circuits which may lead to damage to the insulation of a motor or a TL [14]–[22].

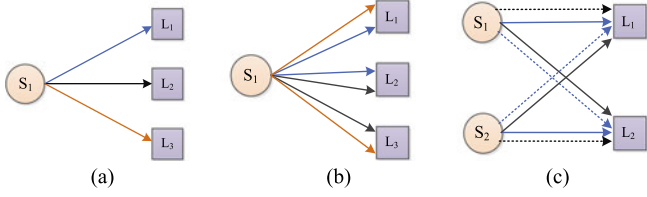


Fig. 3. HFDPS. (a) SISO, (b) SIMO, and (c) MIMO network topologies. The links marked with same colors can transfer power simultaneously while dotted lines in (c) show the interference (leakage) path for power.

One way to mitigating the TL effect is via active compensation along the TL [30]–[32], which ensures signal integrity for a wide range of frequency of wave transmission. However, such an active-compensation scheme is often limited by an increase in the associated cost and complexity of the compensated system. Therefore, it is preferred to design an alternative strategy to eliminate the TL effects. A unique approach was presented in [33]–[37] for exploiting the periodicity property exhibited by the input impedance of the TL with varying length of wave transmission. It was demonstrated that, by choosing a particular TL length and keeping the frequency of wave transmission constant, voltage and current profile of a system can be modified in any desired manner. However, such a methodology is not applicable when the length of the TL cannot be varied. Furthermore, past research mainly dealt with single-input and single-output (SISO) HFDPS topologies that lack scalability for single-input and multiple-output (SIMO) and multiple-input and multiple-output (MIMO) HFDPS topologies [33]–[37].

In this paper, to extend the analysis and validate the scalability of SIMO and MIMO HFDPS topologies as illustrated in Fig. 3, we have outlined a methodology for generalized input impedance modeling of spatiotemporal-coupled TL network. Using this methodology, scenario-centric input-impedance model is extracted, which leads to a frequency selection criterion. The frequency selection criterion exploits the periodic property of a TL exhibited by its input impedance as a function of the frequency of wave transmission to ensure the integrity of a power signal being transmitted to an unmatched load in a HFDPS.

This paper is divided into five sections. In Section II, input impedance modeling of a HFDPS with TL network has been outlined. In Section III, various HFDPS topologies are discussed in detail and frequency-selection criterion is derived for each topology. Next, in Section IV, an experimental setup for validation is outlined along with detailing of the experimental results and their analyses. Also, simulated parametric plots are provided for demonstrating the periodic property exhibited by the input impedance for scenario-centric SISO, SIMO, and MIMO topologies. A brief conclusion of our work is outlined in Section V.

II. GENERALIZED INPUT IMPEDANCE MODELING OF A HFDPS WITH TL NETWORK

Fig. 4 illustrates a simplified representation of a generalized HFDPS. Essentially, the HFDPS provides a pathway for power

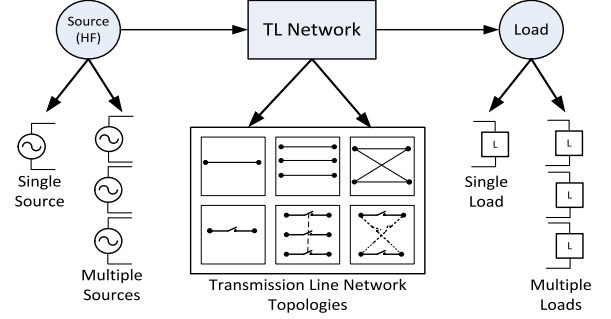


Fig. 4. Illustration of a simplified representation of a HFDPS, which provides a power-transfer pathway between the energy source(s) and load(s) (which may/may not be monolithic) over a TL network that may have a singular/plural path-invariant/path-varying TL(s).

transfer between energy source(s) and application load(s) over a TL network that may have a singular/plural path-invariant/path-varying TL(s). Such a HFDPS may have multiple topological manifestations including SISO, SIMO, and MIMO topologies. Furthermore, the load in Fig. 4 may not be a monolithic load. Thus, a generalized analysis of n number of sources feeding n number of loads simultaneously through a TL network, as shown in Fig. 4, is provided. The TL network is composed of n spatiotemporal-coupled TL(s).

Starting from n mutually coupled TLs of different characteristics, TL equations in a matrix form is written as

$$\partial_z V = -L \partial_t I \quad (1)$$

$$\partial_z I = -C \partial_t V \quad (2)$$

where ∂_z and ∂_t are the partial differential operators w.r.t. space and time, respectively. Also V, I are $n \times 1$ voltage and current column vectors and are represented as $V = [v_1 \dots v_n]^T$ and $I = [i_1 \dots i_n]^T$. Symbols L and C are matrices of order $n \times n$. The principal diagonal elements of L and C matrices are L_{jk} and C_{jk} , where $(j = k)$ represents self-inductance and capacitance per unit length of individual TL while off diagonal elements L_{jk} and C_{jk} , where $(j \neq k)$ represent mutual inductance and mutual capacitance per unit length between TLs in the TL network. To study the input impedance as seen by the sources $S_1 S_2 \dots S_n$, an equivalent form of (1) and (2) in frequency domain is written as follows:

$$\partial_z V = -j X_L I \quad (3)$$

$$\partial_z I = -j X_C V \quad (4)$$

where X_L and X_C are $n \times n$ matrices and are represented as

$$X_L = \begin{bmatrix} \omega_1 L_{11} & \dots & \omega_n L_{1n} \\ \vdots & \ddots & \vdots \\ \omega_1 L_{n1} & \dots & \omega_n L_{nn} \end{bmatrix}, \quad X_C = \begin{bmatrix} \omega_1 C_{11} & \dots & -\omega_n C_{1n} \\ \vdots & \ddots & \vdots \\ -\omega_1 C_{n1} & \dots & \omega_n C_{nn} \end{bmatrix}.$$

On differentiating (3) with respect to ∂_z and subsequent substitution of (4) in (3), one obtains the following expression:

$$\partial_z^2 V + X_L X_C V = 0 \quad (5)$$

$$\partial_z^2 I + X_L X_C I = 0. \quad (6)$$

The matrix $X_L X_c$ is of order $n \times n$ and has distinct eigenvalues $\beta_1 \beta_2 \dots \beta_n$. For such a matrix, eigenvectors $p_1, p_2 \dots, p_n$ corresponding to $\beta_1, \beta_2 \dots, \beta_n$ will be linearly independent and can be used to yield a diagonal matrix D :

$$D = P(X_L X_c)P^{-1} = \text{diag}[\beta_1 \dots \beta_n]. \quad (7)$$

In (5) and (6), since matrix $X_L X_c$ couples each element of $(\partial_z^2 V, \partial_z^2 I)$ to each element of (V, I) , respectively, a decoupled system of equations is generated using transformation $U = pV$ and $J = pI$ yielding the following:

$$\partial_z^2 U + D'U = 0 \quad (8)$$

$$\partial_z^2 J + D'J = 0. \quad (9)$$

Solving (8) and (9), one obtains:

$$U = [U_1 \dots U_n]^T \quad (10)$$

$$J = [J_1 \dots J_n]^T \quad (11)$$

where the n th element of U and J are given, respectively, by $U_n^+ e^{-j\sqrt{\beta_n}z} + U_n^- e^{+j\sqrt{\beta_n}z}$ and $J_n^+ e^{-j\sqrt{\beta_n}z} + J_n^- e^{+j\sqrt{\beta_n}z}$.

Now, (10) and (11) can be transformed back to coupled system of equations by using following transformations:

$$V = P^{-1} U \quad (12)$$

$$I = P^{-1} J. \quad (13)$$

If matrix P^{-1} is a $n \times n$ matrix represented by $[p_{jk}]$, where p_{jk} , (12) and (13) are expressed as follows:

$$V = [v_1 \dots v_n]^T \quad (14)$$

$$I = [i_1 \dots i_n]^T \quad (15)$$

and the n th element of V and I are, respectively, given by $p_{n1}U_1 + p_{n2}U_2 + \dots + p_{nn}U_n$ and $p_{n1}J_1 + p_{n2}J_2 + \dots + p_{nn}J_n$. Matrix I can also be expressed in terms of U using (3) as

$$I = jX_L^{-1} \left[\sum_{i=1}^{i=n} p_{1i}(\partial_z U_i) \dots \sum_{i=1}^{i=n} p_{ni}(\partial_z U_i) \right]^T. \quad (16)$$

Equations (14) and (16) represent voltage and current at any z on a TL in a n spatiotemporal-coupled TL network.

For simplification, n spatiotemporal-coupled TL(s) are assumed to have same characteristics such that the principal diagonal elements of matrix L and C are equal, i.e., $L_{jk} = L$ and $C_{jk} = C$, where $(j = k)$. Furthermore, it is assumed that the off diagonal elements of matrix L and C are equal, i.e., $L_{jk} = L_m$ and $C_{jk} = C_m$, where $(j \neq k)$. Thus, using (14) and (16) the voltage and current at any point z on n th TL in a n spatiotemporal-coupled TL network can be represented as

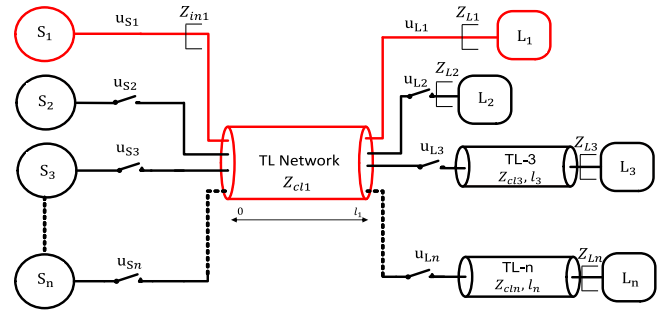


Fig. 5. SISO power transfer for a HFDPS. The TL network can be configured to realize multiple other SISO realizations by connecting any one source to any one load with/without a preceding TL.

follows:

$$v_n = \left[\sum_{m=1}^n p_{nm} \left(U_m^+ e^{-j\sqrt{\beta_m}z} + U_m^- e^{+j\sqrt{\beta_m}z} \right) \right] \quad (17)$$

$$i_n = j \begin{bmatrix} c_{11} & \dots & c_{12} \\ \vdots & \ddots & \vdots \\ c_{12} & \dots & c_{11} \end{bmatrix} \left[\sum_{m=1}^n p_{nm} \left(U_m^+ e^{-j\sqrt{\beta_m}z} + U_m^- e^{+j\sqrt{\beta_m}z} \right) \right] \quad (18)$$

where $c_{11} = \frac{L+(n-2)L_m}{N_c}$, $c_{12} = \frac{-L_m}{N_c}$, and $N_c = \omega_1((L^2 - (n-1)L_m^2) + (n-2)LL_m)$. On applying boundary conditions at load and source end, input impedance as seen by the source S_n is represented as

$$Z_{inn} = F_n \left(Z_{L1} \dots Z_{Ln}, L, C, \omega_n, \beta_1 \dots \beta_n, l_1 \dots l_n, L_m, C_m \right). \quad (19)$$

A detailed analysis for a 2×2 scenario-centric HFDPS in which two sources S_1 and S_2 feeds two loads L_1 and L_2 via two spatiotemporal-coupled TL(s) is presented in Appendix A. Following the methodology presented in Section II, Appendix A further details the expression of the input impedance as seen by S_1 and S_2 .

III. INPUT-IMPEDANCE-BASED FREQUENCY-DEPENDENT CRITERIA FOR TL-NETWORK-BASED HFDPS TOPOLOGIES

Analyses of three distinct scenario-centric HFDPS topologies are conducted next using input-impedance modeling methodology provided in Section II. They lead to corresponding frequency-selection criteria that ensure the integrity of the transmitted signal under periodic condition.

A. Case A: HFDPS With SISO Topology

Fig. 5 shows a HFDPS with a pathway marked in red, illustrating a SISO power transfer originating at a single source (S_1) and terminating at a single load (L_1) with an impedance of Z_{L1} by closing the source and load-side switches u_{S1} and u_{L1} , respectively. It is noted that a SISO realization for the HFDPS can be obtained in several other ways by linking any one source to any one load with/without a preceding TL. For these scenarios,

the scenario-centric analysis carried out next is applicable with small variations that will be outlined at the end of the analysis.

As mentioned earlier, we assume that S_1 is connected to L_1 (with an impedance of Z_{L1}) via the TL network of length l_1 . Furthermore, let Z_{in1} represent the impedance reflected at the input (or source-end) of the SISO topology as illustrated in Fig. 5. If there is no mutual coupling between the TL(s) in TL network such that $L_m = 0$ and $C_m = 0$, then using (A3), as provided in Appendix A, input impedance as seen by the source S_1 for SISO topology is given as follows:

$$Z_{in1} = \frac{\left[(Z_{L1}) + j\sqrt{L/C} \tan\left(2\pi f_1 \sqrt{LC} l_1\right) \right] \sqrt{L/C}}{\left(\sqrt{L/C} + jZ_{L1} \tan\left(2\pi f_1 \sqrt{LC} l_1\right) \right)}. \quad (20)$$

It is important to note that substitution of $f_1 = n/2\sqrt{LC}l_1$ (where n is an integer) in (20) always yields

$$Z_{in1} = Z_{L1}. \quad (21)$$

For any other frequency of wave transmission that does not satisfy $f_1 = n/2\sqrt{LC}l_1$, (20) is not satisfied as well. Instead, Z_{in1} could exhibit resistive or reactive impedance for the same load [38], [39]. Above outlined hypothesis can be extended to other cases with minor adjustments. For instance, if one considers that S_1 has to transfer power to L_3 which is preceded by an additional TL (TL-3), the same procedure can be followed in two steps. First, a set of frequencies ($f_3 = n/2\sqrt{LC}l_3$) have to be determined using parameters of TL-3 and then a subset of the obtained frequency set ($f_1 \subseteq f_3$) is to be established using the parameters of the TL network such that the input impedance (Z_{in1}) becomes equal to the load impedance (Z_{L3}). Similar analysis can also be applied if air is chosen as the transmission medium instead of a waveguide. The difference will appear in the obtained set or subset of frequencies as L and C assume different values for air.

B. Case B: HFDPS With SIMO Topology

In Fig. 6, the section of the HFDPS marked in red illustrates a SIMO topology. It comprises S_1 that feeds power to L_1 and L_3 over the TL network. While L_1 is directly connected to the TL network of length l_1 , L_3 is connected to the TL network via a TL marked TL-3 of length l_3 . Similar to Case A, a SIMO topology can be obtained in plurality of ways by connecting any single source to multiple loads among L_1 through L_n with or without a preceding TL. It is assumed that the TL network and TL-3 have same characteristics. For the illustrated SIMO topology, if coupling between the TLs in TL network is assumed to be zero, then using (A3), the input impedance (Z_{in1}) as seen by S_1 is given by (22), shown at the bottom of this page.

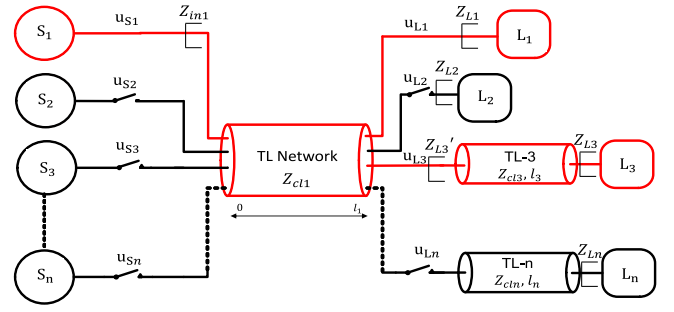


Fig. 6. Illustration of a SIMO topology marked in red. It comprises S_1 that feeds L_1 and L_3 over the TL network; L_1 is directly connected to the TL network and L_3 is connected to the TL network via a TL-3.

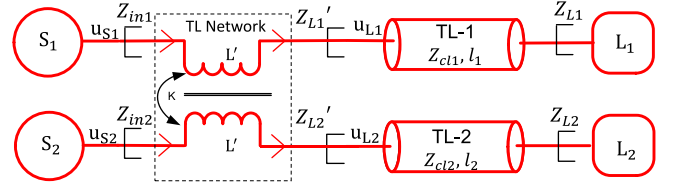


Fig. 7. Simple embodiment of crosstalk in a MIMO topology with TL network replaced with a coupled inductor.

It is important to note that, in (22), substitution of $f_1 = \frac{n}{2\sqrt{LC}l_1} = \frac{m}{2\sqrt{LC}l_3}$ (where m is an integer) always yields

$$Z_{in1} = Z_{L1} * Z_{L3} / Z_{L1} + Z_{L3}. \quad (23)$$

Following Case A, for a given l_1 and l_3 , if the frequency of wave transmission is so selected such that $f_1 = \frac{nv}{2l_1} = \frac{mv}{2l_3}$, then (23), which represents the impedance matching condition, is satisfied. The latter ensures signal integrity by mitigating the TL effects between S_1 and L_1 and L_3 . For any other frequency of wave transmission, (23) is not satisfied. It is noted that the outlined approach is applicable for any other SIMO topology shown in Fig. 6 and even if air instead of a conductive waveguide is the medium of transmission.

C. Case C: HFDPS With MIMO Topology

While several HFDPSs may emulate SISO and SIMO topologies, MIMO topologies, which involve simultaneous power transfer from a plurality of sources to a plurality of loads, is often a reality. Consider a scenario in Fig. 7, where S_1 and S_2 transfers power to load L_1 and L_2 simultaneously, as a result of cross-coupling between the TLs in the TL network, a part of S_1 's (S_2 's) power is fed to L_2 (L_1), which is undesirable. Crosstalk in a MIMO topology due to a finite mutual coupling between the TL(s) can be understood in the form of either spatiotemporal (distributive coupling) coupling as presented in Appendix A or a temporal coupling for a 2×2 HFDPS

$$Z_{in1} = \sqrt{\frac{L}{C}} \left[\frac{\left\{ \frac{(Z_{L1}Z_{L3}(\sqrt{L/C}) + jZ_{L1}(L/C)\tan(2\pi f_1\sqrt{LC}l_3))}{(\sqrt{L/C})(Z_{L1}+Z_{L3}) + j\tan(2\pi f_1\sqrt{LC}l_3)(Z_{L2}+(L/C))} \right\} + j\sqrt{L/C} \tan\left(2\pi f_1 \sqrt{LC} l_1\right)}{j \left\{ \frac{(Z_{L1}Z_{L3}(\sqrt{L/C}) + jZ_{L1}Z_{cl}^2 \tan(2\pi f_1 \sqrt{LC} l_2)) \tan(2\pi f_1 \sqrt{LC} l_1)}{\sqrt{L/C}(Z_{L1}+Z_{L3}) + j \tan(2\pi f_1 \sqrt{LC} l_3)(L/C) + Z_{L1}Z_{L3}} \right\} + \sqrt{L/C}} \right] \quad (22)$$

as shown in Fig. 7. The generalized and case specific analysis for the spatiotemporal-coupled TL is provided in Section II and Appendix B, respectively. This section is attributed to the scenario-centric analysis for a finite mutual temporal coupling represented by coupled inductor as shown in Fig. 7. TL-1 and TL-2 are assumed to have the same characteristics.

Using the input impedance expression as obtained in case A for the SISO topology, Z_{L_1}' and Z_{L_2}' are given by

$$Z_{L_1}' = \frac{\left[(Z_{L_1}) + j\sqrt{L/C} \tan\left(2\pi f_1 \sqrt{LC}l_1\right) \right] \sqrt{L/C}}{\left(\sqrt{L/C} + jZ_{L_1} \tan\left(2\pi f_1 \sqrt{LC}l_1\right) \right)} \quad (24)$$

$$Z_{L_2}' = \frac{\left[(Z_{L_2}) + j\sqrt{L/C} \tan\left(2\pi f_2 \sqrt{LC}l_2\right) \right] \sqrt{L/C}}{\left(\sqrt{L/C} + jZ_{L_2} \tan\left(2\pi f_2 \sqrt{LC}l_2\right) \right)}. \quad (25)$$

To calculate the input impedance seen by S_1 , S_2 is short-circuited such that $v_{in2} = 0$. This yields Z_{in1} as given by (26), shown at the bottom of this page.

Similarly, Z_{in2} as seen by S_2 can be calculated by short circuiting S_1 such that $v_{in1} = 0$ and is given by (27), shown at the bottom of this page, where M represents the mutual inductance between the two temporally coupled TL(s) in the TL network and its expression is given by $M = KL'$, K being the mutual coupling coefficient. To ensure signal integrity, the following conditions need to be satisfied:

1)

$$Z_{in1} = Z_{L_1} + j\omega_1 L', \quad Z_{in2} = Z_{L_2} + j\omega_2 L'. \quad (28)$$

2) Signal-to-interference-noise ratio (SINR) should be high.

One way to practically satisfy both conditions is to ensure negligible K for the system and chose frequency of wave transmission $f_1 = \frac{n}{2\sqrt{LC}l_1}$ and $f_2 = \frac{m}{2\sqrt{LC}l_2}$. However, for large value

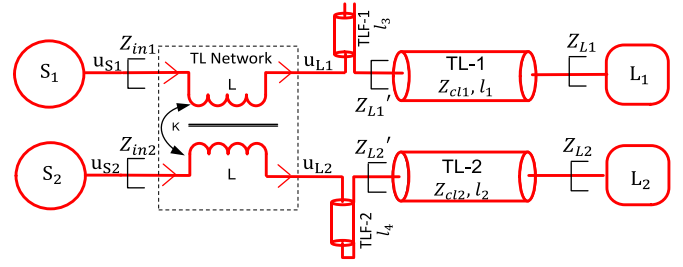


Fig. 8. Mitigation of crosstalk using tuned TL-based band-stop filters TLF-1 and TLF-2.

of K , using the frequency set $f_1 = \frac{n}{2\sqrt{LC}l_1}$ and $f_2 = \frac{m}{2\sqrt{LC}l_2}$ alone will not ensure signal integrity. An alternative approach to ensure signal integrity in a MIMO topology, as shown in Fig. 8, is to use a band-stop filter in the power transmission path between S_1 (S_2) and L_1 (L_2). We use a TL-based band-stop filter [26], outlined in Appendix B, to exploit the periodic property of such a filter. The basic idea, following Case A, is to initially select a set of frequencies of wave transmission between S_1 (S_2) and L_1 (L_2) such that the condition for signal integrity following (28) is achieved assuming no crosstalk. Next, the band-stop filter for each of these paths is placed and so tuned so that they only let go the power signal at the selected frequency of wave transmission. Thus, for the MIMO topology, any cross talk between S_1 (S_2) and L_2 (L_1) is essentially eliminated and power flows from S_1 (S_2) and L_1 (L_2) without signal-integrity issues.

IV. RESULTS

An experimental setup, shown in Fig. 9, is developed to conduct experimental validations of the frequency-selection criterion outlined in Section III and extended for SISO, SIMO, and MIMO topologies. Frequency-domain experimentations and validations are carried out using an HP3577A vector network analyzer (VNA). The HP 35677A S-parameter test set

$$Z_{in1} = \left(\frac{\left[(Z_{L_1}) + j\sqrt{L/C} \tan\left(2\pi f_1 \sqrt{LC}l_1\right) \right] \sqrt{L/C}}{\left(\sqrt{L/C} + jZ_{L_1} \tan\left(2\pi f_1 \sqrt{LC}l_1\right) \right)} + j\omega_1 L' \right) + \left(jM\omega_1 \frac{\left[\frac{\left[(Z_{L_2}) + j\sqrt{L/C} \tan\left(2\pi f_1 \sqrt{LC}l_2\right) \right] \sqrt{L/C}}{\left(\sqrt{L/C} + jZ_{L_2} \tan\left(2\pi f_1 \sqrt{LC}l_2\right) \right)} + j\omega_1 (L' - M) \right]}{\left(\frac{\left[(Z_{L_2}) + j\sqrt{L/C} \tan\left(2\pi f_1 \sqrt{LC}l_2\right) \right] \sqrt{L/C}}{\left(\sqrt{L/C} + jZ_{L_2} \tan\left(2\pi f_1 \sqrt{LC}l_2\right) \right)} + jL'\omega_1 \right)} - j\omega_1 M \right) \quad (26)$$

$$Z_{in2} = \left(\frac{\left[(Z_{L_2}) + j\sqrt{L/C} \tan\left(2\pi f_2 \sqrt{LC}l_2\right) \right] \sqrt{L/C}}{\left(\sqrt{L/C} + jZ_{L_2} \tan\left(2\pi f_2 \sqrt{LC}l_2\right) \right)} + j\omega_2 L' \right) + \left(jM-\omega_2 \frac{\left[\frac{\left[(Z_{L_1}) + j\sqrt{L/C} \tan\left(2\pi f_2 \sqrt{LC}l_1\right) \right] \sqrt{L/C}}{\left(\sqrt{L/C} + jZ_{L_1} \tan\left(2\pi f_2 \sqrt{LC}l_1\right) \right)} + j\omega_2 (L' - M) \right]}{\left(\frac{\left[(Z_{L_1}) + j\sqrt{L/C} \tan\left(2\pi f_2 \sqrt{LC}l_1\right) \right] \sqrt{L/C}}{\left(\sqrt{L/C} + jZ_{L_1} \tan\left(2\pi f_2 \sqrt{LC}l_1\right) \right)} + jL'\omega_2 \right)} - j\omega_2 M \right) \quad (27)$$

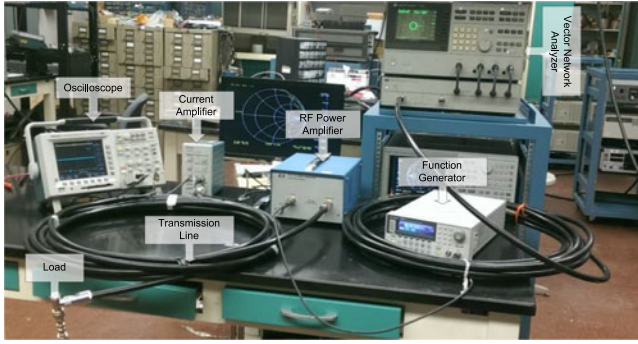


Fig. 9. Experimental setup for validating frequency-selection criterion.

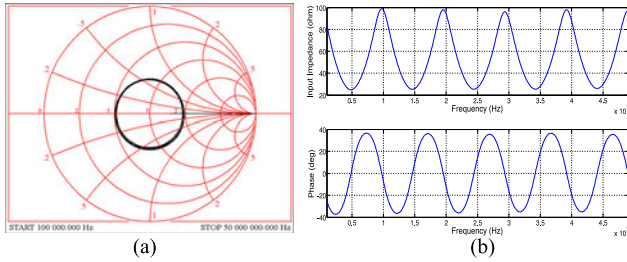


Fig. 10. Experimental results showing (a) variation in the input impedance with frequency of wave transmission for SISO topology (marked in red in Fig. 5) and (b) magnitude and phase variations of the input impedance with frequency for the same SISO topology.

is used to study the scattering (S) parameters [28] of the TL network (see Figs. 5–7) for the various network topologies. A Belden 7977A coaxial cable has been chosen as the TL (with following parameters: characteristic impedance: 50Ω , inductance: $0.1968 \mu\text{H}/\text{m}$, capacitance: $80.688 \text{ pF}/\text{m}$, velocity of propagation: 84% , delay: $3.96 \text{ ns}/\text{m}$, and dc resistance: $11.7384 \text{ m}\Omega/\text{m}$) and Bourns radio-frequency (RF) resistive loads have been used. Time-domain analyses are carried out at a frequency of 10 MHz to limit the size of the experimental setup. An RF power amplifier (ENI 503L from Bell Electronics) is used to generate the HF power signals.

Fig. 10(a) shows the variation of the input impedance with frequency of wave transmission using a Smith chart for the SISO topology marked in red in Fig. 5. It can be seen from the Smith chart that the input impedance varies between 0.5 – 2 p.u. of the characteristic impedance, which corresponds to a range of 25 – 100Ω . Furthermore, even though the input impedance is purely resistive at integer multiples of 5 MHz , it matches the load impedance of 100Ω only at integer multiples of 10 MHz . At odd integral multiples of 5 MHz , which according to (20) yields an input impedance of $Z_{\text{in}1} = L/CZ_L = 25 \Omega$ and is shown by the intersection of the circle with the Smith's chart at 0.5 on the horizontal axis.

The magnitude and phase variations of the input impedance as a function of the frequency of wave transmission for the SISO topology (see Fig. 5) are shown in Fig. 10(b). Following [28], the data points for Fig. 10(b) are extracted from the S_{11} parameter obtained using the VNA. Fig. 10(b) shows that, at integral multiples of 5 and 10 MHz , the input impedance is resistive in nature indicated by zero phase angles; however, its magni-

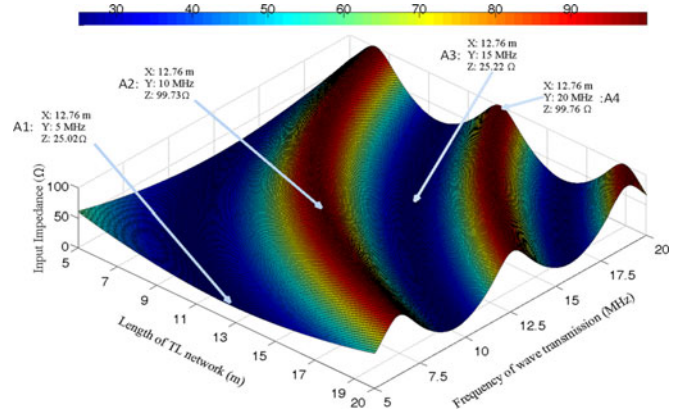


Fig. 11. Variation in input impedance with frequency of transmission and TL network length for a SISO topology. TL length, the frequency of transmission, and input impedance are marked by X, Y, and Z, respectively.

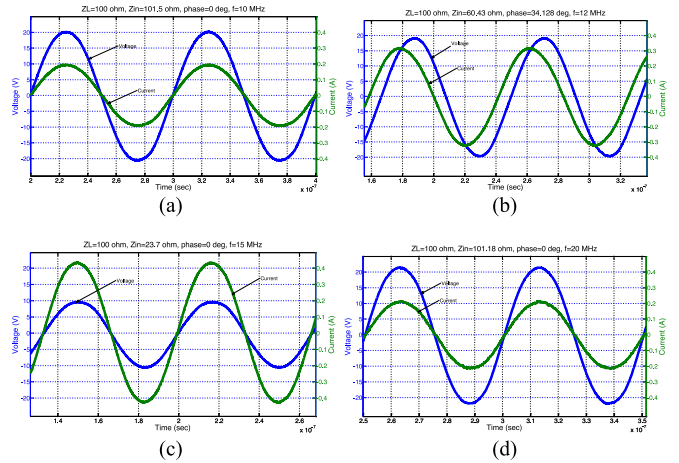


Fig. 12. Experimental input voltage and current for the SISO topology (see Fig. 5) at (a) 10 , (b) 12 , (c) 15 , and (d) 20 MHz .

tude matches the load impedance only at integral multiples of 10 MHz . It can also be observed that the input impedance shows a periodic nature and follows our simulation result in Fig. 11 for a TL-network length of 12.75 m .

Fig. 12 displays the time-domain results for the same SISO topology. The designed setup was tested at 10 , 12 , 15 , and 20 MHz . At 10 , 15 , and 20 MHz , the voltage and current at the input of the TL network are in phase but the input impedance closely matches the load impedance ($Z_{L1} = 100 \Omega$) only at 10 and 20 MHz . This is because for propagation velocity of 84% (see Table I) and TL network length of 12.75 m , (21) is satisfied only at input wave frequencies that are integer multiples of 10 MHz . However, at 15 MHz the present length of TL network (12.75 m) is equivalent to $3\lambda/4$, and the input impedance is found to be $Z_{\text{in}1} = L/CZ_{L1} = 23.7 \Omega$. At a frequency of 12 MHz , the input impedance is found to be inductive in nature and does not match the load impedance. The time-domain results obtained in Fig. 12 closely match the simulation result shown in Fig. 11 for a TL network length of 12.75 m and frequency-domain results in Fig. 10(a) and (b). This serves as a clear proof for the SISO frequency-selection criterion provided in Section III.

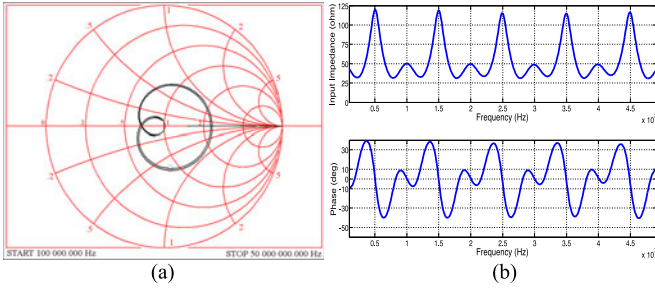


Fig. 13. Experimental variation in the (a) input impedance and (b) magnitude and phase variations of the input impedance with frequency of wave transmission for the SIMO topology marked in red in Fig. 6.

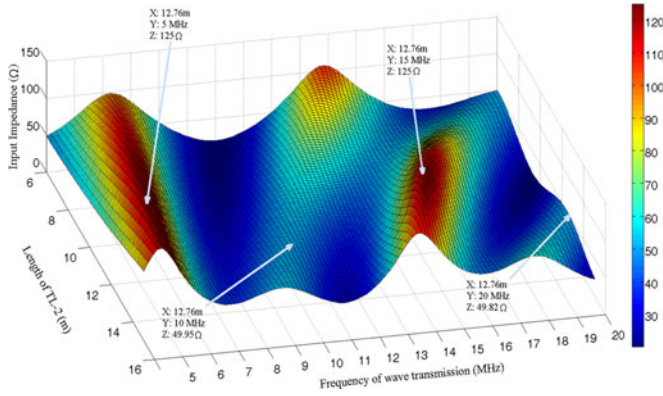


Fig. 14. Variation in input impedance with variation in frequency of wave transmission and TL-3 length for the SIMO topology marked in red in Fig. 6. TL-network length is marked by X, the frequency of wave transmission is marked by Y and input impedance is marked with Z.

Frequency-domain results for the SIMO topology marked in red in Fig. 5 are presented in Fig. 13(a) in the form of Smith's chart and in Fig. 13(b) as magnitude and phase plots. Both the TL network and TL-3 were chosen to have a length of 12.75 m and L_1 and L_3 were chosen to be 100 Ω each. It can be observed from the Smith chart as shown in Fig. 13(a) that the input impedance curve intersects the horizontal axis at 0.66, 1, and 2.46 p.u. of the characteristic impedance. This signifies a resistive input impedance of 33, 50, and 123 Ω , respectively. Similar results can also be inferred from the frequency-domain results shown in Figs. 13(b). It is noted that in Fig. 13(a) and (b) the magnitude of input impedance decreases in successive cycles as a result of lossy TL characteristics. At odd integer multiple of 5 MHz, the input impedance is resistive in nature and approaches 125 Ω . However, at integer multiples of 10 MHz, using (22) the value of the input impedance is given by the parallel combination of Z_{L1} and Z_{L3} and approaches 50 Ω . As can be inferred from Fig. 13(b), in a single period there are four points on the graph at which phase angle is zero. The input impedance at these points can be calculated using (22) by equating the imaginary part of Z_{in1} to zero.

Frequency-domain and simulation results for the SIMO topology are provided in Figs. 13 and 14, respectively. These are also validated by the time-domain results as shown in Fig. 15 for TL-3 of length 12.75 m. Fig. 13 displays that at 10 and 20 MHz

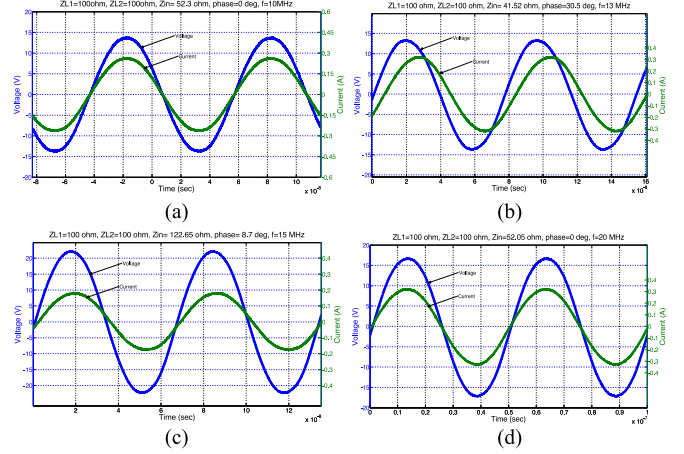


Fig. 15. Experimental input voltage and input current for the SIMO topology at (a) 10, (b) 12, (c) 15, and (d) 20 MHz.

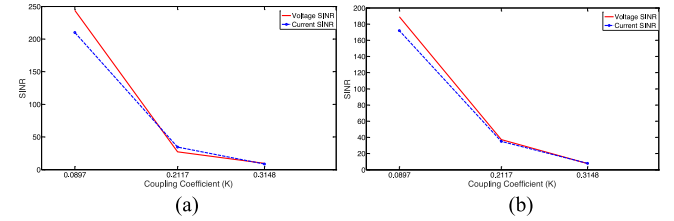


Fig. 16. Variations in experimental SINRs of the voltage and current as a function of K . At the input of (a) TL-1 and (b) TL-2 having fundamental component of 10 MHz with a 20 MHz noise frequency.

the input impedance is resistive in nature and has a magnitude close to 50 Ω that satisfies (23). Also, at 15 MHz the input impedance is still resistive in nature; however, at this frequency, the magnitude of the input impedance is 122.65 Ω which matches the frequency-domain results provided in Fig. 13. Likewise, it can be observed that at 13 MHz, the input impedance is inductive in nature which follows from (22). These results provide a proof for the SIMO frequency selection criterion provided in Section II.

Next, an experimental setup was developed for ascertaining the validity of (28) for power flow in the MIMO topology as shown in Fig. 7. Condition (28) is satisfied by setting frequencies of wave transmissions or signal frequencies corresponding to S_1 and S_2 to be 10 and 20 MHz, respectively. This ensures, following Case A and in the absence of crosstalk, mitigation of noise in the transmitted power signals being fed to two 100 Ω loads through two temporal-coupled TL(s) each with a physical length of 12.75 m. Fig. 16 demonstrates the variation in the SINR of voltage and current as a function of K . Due to coupling in the TL network, the crosstalk noise frequency for the path between S_1 and L_1 and S_2 and L_2 are found to be 20 and 10 MHz, respectively. It is evident from Fig. 16 that the SINR increases as K is decreased because with progressively lower values of K , Z_{in1} , and Z_{in2} in (26) and (27) approaches (28), thereby further reducing the impact of crosstalk noise.

To satisfy (28), we pursue an alternate approach by placing band-stop filters, tuned at band-stop frequencies of 20 and 10 MHz, in the paths between S_1 and L_1 and S_2 and L_2 ,

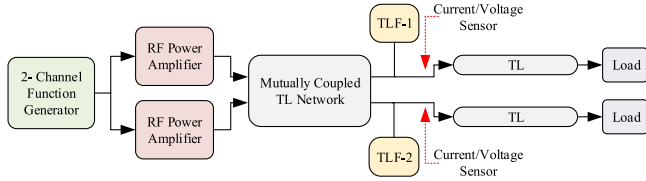


Fig. 17. Mitigation of crosstalk in Fig. 7 using tuned TL-based band-stop filters TLF-1 and TLF-2.

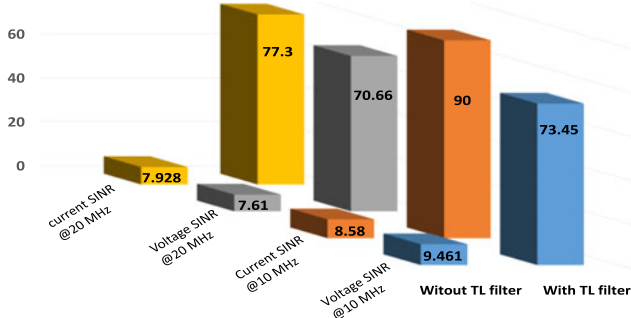


Fig. 18. Comparison of experimentally obtained SINRs with and without the band-stop filter for the MIMO topologies in Figs. 7 and 8.

respectively. Fig. 17 captures the flow of the experimental setup that is used to investigate the impacts of adding TL filters (TLF-1 and TLF-2) on SINR of current and voltage signals. For simplicity, the band-stop filter was designed using TL, as outlined in Appendix B. Fig. 18 compares the variation in SINR for $K = 0.3148$ with and without the use of band-stop filters. The results show a significant improvement in SINR for both the current and voltage waveforms at the input of TL-1 and TL-2.

Finally, we explore the impact of transmitting a periodic signal synthesized using a plurality of frequencies in the presence of TL effect. It is demonstrated that, if the selection of these frequency components of the time-domain signal are carefully selected then, the impact of TL effect is mitigated. Even though we demonstrate the outcome of the analysis for the SISO topology shown in Fig. 5, the concept extends to SIMO and MIMO cases as well. To ensure the integrity of the transmitted power signal in a SISO topology, the frequency of wave transmission must satisfy condition (21), which, as outlined in Section II, yields a set of discrete frequencies that exhibit a periodic property. So, instead of transmitting a signal comprising only one of these discrete frequency components, if a signal comprising a plurality of these discrete-frequency components is transmitted, then one can expect no signal-integrity issue in the power signal as well. Fig. 19 shows the outcome of such a prediction using a bipolar square-wave signal (of 0.5 duty ratio) that has a fundamental frequency of 10 MHz and superharmonics that are multiples of 10 MHz yielding $V(t) = \sum \frac{4V_p}{(2N-1)\pi} \sin(2N-1)\omega t$, where V_p represents the peak voltage of the square wave and N represents consecutive positive integer with an initial value of 1. It is noted that the 10 MHz frequency component and the superharmonics are chosen from a set that satisfy (21). In Fig. 19, rms voltage of each harmonic component at the source is plotted for two cases: one when the signal is sent through a TL network of length 12.75 m and the other when no TL network is used. It is

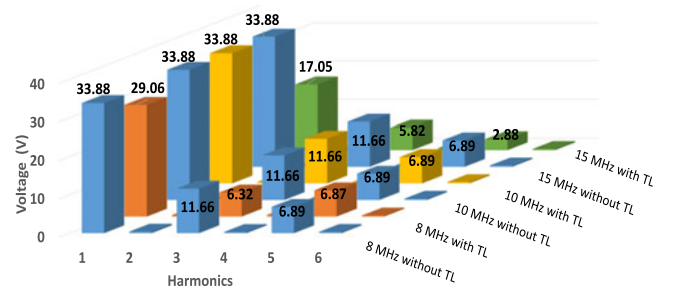


Fig. 19. Experimental result showing comparison of harmonic-voltage components when a square wave is transmitted in the absence or presence of TL effect.

apparent from Fig. 19 that, and as expected, for the case under consideration, the magnitudes of the harmonic components for these two cases do not show any significant difference. However, when the two scenario-centric analyses were repeated for 8 and 15 MHz base frequency of the bipolar square wave, a tangible difference was observed in the amplitudes of the base and superharmonic-frequency components. This is because both 8 and 15 MHz base frequency and their superharmonic components do not satisfy the impedance criterion (21).

V. CONCLUSION

The maturity of standalone high-frequency power electronics has opened the possibility for HFDPSs, which have the potential for yielding multipronged advantages including high power density, rapid power flow, reduced localized storage requirements, and high network control bandwidth. However, distribution of high-frequency power signals over a HFDPS (that may assume SISO, SIMO, and MIMO topologies) brings forth the increasing possibility of encountering TL effects that can yield poor signal quality. At the printed-circuit-board level, such TL effects have been addressed by using active-compensation techniques or by adjusting the physical length of the TL.

In contrast, in this paper, using generalized input-impedance modeling of SISO/SIMO/MIMO HFDPS, we have explored frequency as the modulation parameter for addressing the TL effects. The applicability of the outlined analysis was not limited to fixed type and magnitude of the impedances. To determine frequency sets that ensure signal integrity in presence of TL effects, a generalized input impedance modeling for n mutually coupled TLs was presented. Next, the generalized input impedance expression was simplified for a 2×2 HFDPS as shown in Appendix A. Using this input impedance expression, frequency sets that ensure signal integrity were calculated. With regard to the overall analysis, we observed that the procedure for determining the frequency set that ensures impedance criterion for SISO and SIMO topologies remain essentially the same, while for the MIMO topology, an additional criterion that requires mitigating the crosstalk or high SINR needs to be addressed. Two mechanisms for mitigation of the crosstalk noise were explored: one that is based on reducing the coupling strength among the transmission channels while the other is based on using band-stop filters to mitigate the crosstalk noise. Finally, we illustrated a bipolar time-domain square-wave signal

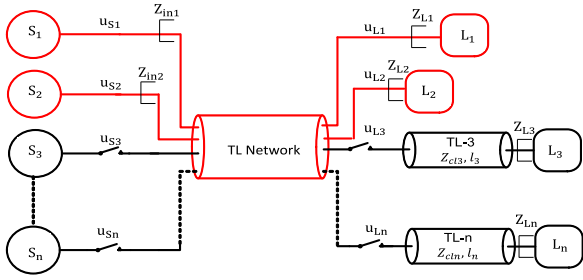


Fig. 20. MIMO topology showing activation of sources and loads.

synthesized using a discrete set of frequencies that individually satisfy the impedance-matching condition for a SISO topology also mitigates the TL effect.

APPENDIX A

For a 2×2 HFDPS, where two sources S_1 and S_2 feed two loads L_1 and L_2 via two spatiotemporal-coupled TLs of length l_1 and l_2 represented by TL network as shown in Fig. 20, using (17) and (18), voltages and currents at any point z on the TL network are given by the following steps:

$$V = [v_1 \ v_2]^T = [p_{11}\sigma_1 + p_{12}\sigma_2 \ p_{21}\sigma_1 + p_{22}\sigma_2]^T \quad (\text{A1})$$

$$I = [i_1 \ i_2]^T = \begin{bmatrix} \frac{\sqrt{\beta_1}(Lp_{11}-p_{21}L_m)\sigma_3 + \sqrt{\beta_2}(Lp_{12}-p_{22}L_m)\sigma_4}{(L^2-L_m^2)\omega_1} \\ \frac{\sqrt{\beta_1}(Lp_{21}-p_{11}L_m)\sigma_3 + \sqrt{\beta_2}(Lp_{22}-p_{12}L_m)\sigma_4}{(L^2-L_m^2)\omega_1} \end{bmatrix} \quad (\text{A2})$$

where

$$\begin{aligned} \sigma_1, \sigma_3 &= U_1^+ e^{-j\sqrt{\beta_1}z} \pm U_1^- e^{+j\sqrt{\beta_1}z} \\ \sigma_2, \sigma_4 &= U_2^+ e^{-j\sqrt{\beta_2}z} \pm U_2^- e^{+j\sqrt{\beta_2}z}. \end{aligned}$$

Symbols $\sqrt{\beta_1}$ and $\sqrt{\beta_2}$ represent propagation constant of individual TL(s) in a coupled TL network. The description of notations $\beta_1, \beta_2, p_{11}, p_{12}, p_{21}, p_{22}$ are given below:

$$\begin{aligned} \beta_1, \beta_2 &= \frac{1}{2}(LC\omega_1^2 - 2C_m L_m \omega_1 \omega_2 + CL\omega_2^2 \\ &\pm \sqrt{(LC\omega_1^2 - CL\omega_2^2)^2 + 4\omega_1 \omega_2 (CL_m \omega_1 - LC_m \omega_2) \\ &\quad (-LC_m \omega_1 + CL_m \omega_2)}) \end{aligned}$$

$$p_{11} = -p_{21} - \omega_1 (CL_m \omega_1 - LC_m \omega_2) / N$$

$$p_{12}, p_{22} = -\frac{-CL\omega_1^2 + CL\omega_2^2 \pm N}{2N}$$

where

$$N = \sqrt{\begin{aligned} &C^2 L^2 \omega_1^4 - 4CLC_m L_m \omega_1^3 \omega_2 - 2C^2 L^2 \omega_1^2 \omega_2^2 \\ &+ 4L^2 C_m^2 \omega_1^2 \omega_2^2 + 4C^2 L_m^2 \omega_1^2 \omega_2^2 - 4CLC_m L_m \omega_1 \omega_2^3 \\ &+ C^2 L^2 \omega_2^4 \end{aligned}}$$

To calculate the input impedance as seen by the sources S_1 and S_2 , the following steps were carried out.

- 1) Using initial conditions on (17) and (18) at $z = 0$ (input of TL-2 and TL-3, respectively), constants $U_1^+, U_1^-, U_2^+, U_2^-$ can be calculated in terms of $i_{L1}, i_{L2}, Z_{L1}, Z_{L2}$;

- 2) Using boundary conditions at the input, Z_{in1} (Z_{in2}) input impedances seen by S_1 (S_2) when S_2 (S_1) is off are calculated:

$$\begin{aligned} Z_{in1} &= \left(2\omega_1 \left(2j \cos[l\sqrt{\beta_1}] \cos[l\sqrt{\beta_2}] (L^2 - L_m^2) \right. \right. \\ &\quad Z_{L1} Z_{L2} \sqrt{\beta_1} \sqrt{\beta_2} + (L - L_m)(L + L_m) \\ &\quad (Z_{L1} + Z_{L2}) \left(-\cos[l\sqrt{\beta_1}] \sin[l\sqrt{\beta_2}] (L + L_m) \right. \\ &\quad \left. \left. \sqrt{\beta_1} + \cos[l\sqrt{\beta_2}] \sin[l\sqrt{\beta_1}] (-L + L_m) \sqrt{\beta_2} \right) \right. \\ &\quad \left. \omega_1 - 2j \sin[l\sqrt{\beta_1}] \sin[l\sqrt{\beta_2}] (L^2 - L_m^2) \omega_1^2 \right) / \\ &\quad \left(\left(\omega_1 \left(-j Z_{L2} \left(\sin[l\sqrt{\beta_1}] \sin[l\sqrt{\beta_2}] (L + L_m)^2 \right. \right. \right. \right. \\ &\quad \left. \left. \left. \beta_1 - 2 \left(1 + \cos[l\sqrt{\beta_1}] \cos[l\sqrt{\beta_2}] \right) (L^2 - L_m^2) \sqrt{\beta_1} \right. \right. \right. \right. \\ &\quad \left. \left. \left. \sqrt{\beta_2} + \sin[l\sqrt{\beta_1}] \sin[l\sqrt{\beta_2}] (L - L_m)^2 \beta_2 \right) \right. \right. \\ &\quad \left. \left. + 2(L^2 - L_m^2) \left(-\cos[l\sqrt{\beta_1}] \sin[l\sqrt{\beta_2}] (L + L_m) \right. \right. \right. \\ &\quad \left. \left. \left. \sqrt{\beta_1} + \cos[l\sqrt{\beta_2}] \sin[l\sqrt{\beta_1}] (-L + L_m) \sqrt{\beta_2} \right) \omega_1 \right) \right. \\ &\quad \left. + j Z_{L1} \left(-2j Z_{L2} \left(-\cos[l\sqrt{\beta_2}] \sin[l\sqrt{\beta_1}] \right. \right. \right. \\ &\quad \left. \left. \left. (L + L_m) \beta_1 \sqrt{\beta_2} - \cos[l\sqrt{\beta_1}] \sin[l\sqrt{\beta_2}] \right. \right. \right. \\ &\quad \left. \left. \left. (L - L_m) \sqrt{\beta_1} \beta_2 \right) - \left(\sin[l\sqrt{\beta_1}] \sin[l\sqrt{\beta_2}] \right. \right. \right. \\ &\quad \left. \left. \left. (L + L_m)^2 \beta_1 - 2 \left(-1 + \cos[l\sqrt{\beta_1}] \cos[l\sqrt{\beta_2}] \right) \right. \right. \right. \\ &\quad \left. \left. \left. (L^2 - L_m^2) \sqrt{\beta_1} \sqrt{\beta_2} + \sin[l\sqrt{\beta_1}] \sin[l\sqrt{\beta_2}] \right. \right. \right. \\ &\quad \left. \left. \left. (L - L_m)^2 \beta_2 \right) \omega_1 \right) \right) \right). \quad (\text{A3}) \end{aligned}$$

$$\begin{aligned} Z_{in2} &= \left(2(L^2 - L_m^2) \omega_2 \left(-2j \cos[l\sqrt{\beta_1}] \cos[l\sqrt{\beta_2}] Z_{L1} Z_{L2} \right. \right. \\ &\quad \left. \left. \sqrt{\beta_1} \sqrt{\beta_2} + (Z_{L1} + Z_{L2}) \left(\cos[l\sqrt{\beta_1}] \sin[l\sqrt{\beta_2}] \right. \right. \right. \\ &\quad \left. \left. \left. (L + L_m) \sqrt{\beta_1} + \cos[l\sqrt{\beta_2}] \sin[l\sqrt{\beta_1}] (L - L_m) \right. \right. \right. \\ &\quad \left. \left. \left. \sqrt{\beta_2} \right) \omega_2 + 2j \sin[l\sqrt{\beta_1}] \sin[l\sqrt{\beta_2}] (L^2 - L_m^2) \omega_2^2 \right) \right) \\ &\quad / \left(\omega_2 \left(2j (L^2 - L_m^2) Z_{L2} \sqrt{\beta_1} \sqrt{\beta_2} + 2 \cos[l\sqrt{\beta_2}] \right. \right. \\ &\quad \left. \left. (L^2 - L_m^2) \sqrt{\beta_2} \left(-j \cos[l\sqrt{\beta_1}] Z_{L2} \sqrt{\beta_1} \right. \right. \right. \\ &\quad \left. \left. \left. + \sin[l\sqrt{\beta_1}] (L - L_m) \omega_2 \right) + \sin[l\sqrt{\beta_2}] \right. \right. \\ &\quad \left. \left. \left(j \sin[l\sqrt{\beta_1}] Z_{L2} \left((L + L_m)^2 \beta_1 + (L - L_m)^2 \beta_2 \right) \right. \right. \right. \\ &\quad \left. \left. \left. + 2 \cos[l\sqrt{\beta_1}] (L - L_m) (L + L_m)^2 \sqrt{\beta_1} \omega_2 \right) \right) \right) \end{aligned}$$

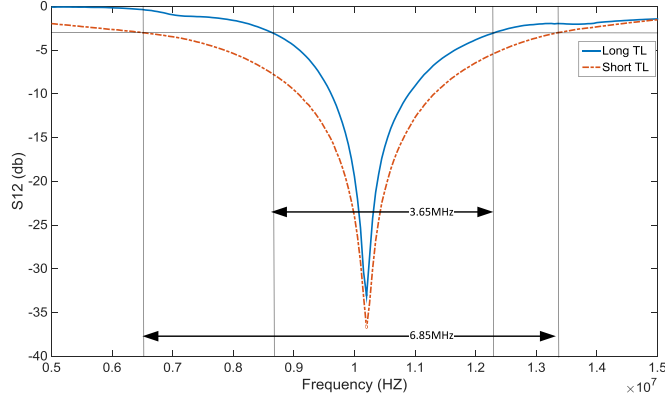


Fig. 21. Experimental result of variation in S_{12} parameter with frequency for TL band-stop filters with different TL lengths.

$$\begin{aligned}
 &+Z_{L1} \left(-2j(L^2 - L_m^2) \sqrt{\beta_1} \sqrt{\beta_2} \omega_2 + 2\cos \left[l\sqrt{\beta_2} \right] \right. \\
 &(L + L_m) \sqrt{\beta_1} \sqrt{\beta_2} \left(\sin \left[l\sqrt{\beta_1} \right] Z_{L2} \sqrt{\beta_1} - j\cos \left[l\sqrt{\beta_1} \right] \right. \\
 &(L - L_m) \omega_2 \left. \right) + \sin \left[l\sqrt{\beta_2} \right] \left(2\cos \left[l\sqrt{\beta_1} \right] (L - L_m) Z_{L2} \right. \\
 &\left. \left. \sqrt{\beta_1} \beta_2 + j\sin \left[l\sqrt{\beta_1} \right] \left((L + L_m)^2 \beta_1 + (L - L_m)^2 \beta_2 \right) \omega_2 \right) \right) \left. \right). \quad (A4)
 \end{aligned}$$

APPENDIX B

Low-, high-, and band-pass and band-stop filters can be designed using a coaxial TL. A TL having length $\lambda/4$ for a frequency behaves as a quarter-wave transformer yielding

$$Z_{in} = Z_{cl} \frac{Z_L + jZ_{cl} \tan(\beta l)}{Z_{cl} + jZ_L \tan(\beta l)}. \quad (B1)$$

Using (B1), when TL of electric length $\lambda/4$ is terminated by an open ($Z_L = \infty$) or short circuit ($Z_L = 0$), the TL input impedance Z_{in} transforms to a short or an open circuit, respectively, for that frequency. In Fig. 8, two TL(s) TLF-1 and TLF-2 are connected to a mutually coupled SISO networks in series with the source as a quarter-wave transformer for 10-MHz signal. The lengths of the TL(s) are chosen such that TLF-1 and TLF-2 have an electric length of $\lambda/4$ for 10 MHz and $\lambda/2$ for 20 MHz. TLF-1 is terminated by an open circuit; hence, it acts as a band-pass filter for 10 MHz and band-stop filter for 20 MHz. TLF-2 is terminated by a short circuit; it acts as band-stop and band-pass filters for 10- and 20-MHz power signals. Using TL configuration evident in Fig. 8, it is ensured that L_1 and L_2 are feed power at 10 and 20 MHz, respectively. A TL filter also exhibits periodic property like a normal TL; hence, TLF-1 and TLF-2 act as band-pass and band-stop filters for frequencies in multiple of $2n - 1$ and $2n$, (where n is an integer), respectively. The bandwidth and attenuation of these TL filters depend on the length of TL being used to design these filters. Fig. 21 displays an experimental comparison between two notch filters of different TL lengths. Dotted and solid curves in Fig. 21 show band-stop filter characteristics for the TL having an electrical length of

$\lambda/4$ and $3\lambda/4$, respectively, for a wave-transmission frequency of 10 MHz. It is observed from Fig. 21 that TL filter of longer length ($3\lambda/4$) has shorter bandwidth (3.65 MHz) and a sharper roll-off; whereas, TL filter of shorter length ($\lambda/4$) has a wider bandwidth (6.85 MHz) with a comparatively gentle roll-off.

REFERENCES

- [1] P. Jain, M. Pahlevaninezhad, S. Pan, and J. Drobnik, "A review of high-frequency power distribution systems: For space, telecommunication, and computer applications," *IEEE Trans. Power Electron.*, vol. 29, no. 8, pp. 3852–3863, Aug. 2014.
- [2] J. Liu, J. Zeng, R. Hu, and K. W. E. Cheng, "A valley-fill driver with current balancing for parallel LED strings used for high-frequency ac power distribution of vehicle," *IEEE Trans. Transp. Electric.*, vol. 3, no. 1, pp. 180–190, Mar. 2017.
- [3] T. Nakamura, G. J. Su, and I. Takahashi, "A 500 Hz power system-microprocessor control of the power converter," in *Rec. KANSAI-section Joint Conv. IEE*, vol. 1, pp. 988–995, 1988.
- [4] I. G. Hansen, "Status of 20 kHz space station power distribution technology," NASA, Washington, DC, USA, Rep. TM 100781, Jan. 1988.
- [5] Y. J. Kim, D. Ha, W. J. Chappell, and P. P. Irazoqui, "Selective wireless power transfer for smart power distribution in a miniature-sized multiple-receiver system," *IEEE Trans. Ind. Electron.*, vol. 63, no. 3, pp. 1853–1862, Mar. 2016.
- [6] A. Musolino, M. Raugi, R. Rizzo, and M. Tucci, "Optimal design of EMALS based on a double-sided tubular linear induction motor," *IEEE Trans. Plasma Sci.*, vol. 43, no. 5, pp. 1326–1331, May 2015.
- [7] Z. Ye, P. K. Jain, and P. C. Sen, "Circulating current minimization in high-frequency ac power distribution architecture with multiple inverter modules operated in parallel," *IEEE Trans. Ind. Electron.*, vol. 54, no. 5, pp. 2673–2687, Oct. 2007.
- [8] S. Lourdes, S. Y. Ng, and P. C. K. Luk, "An alternative power grid-High frequency ac power distribution platforms," in *Proc. IEEE Power Electron. Motion Control Conf.*, 2009, pp. 1949–1956.
- [9] W. A. Fernando and D. D. C. Lu, "Feasibility study of existing 50/60 Hz electrical appliances for HFAC power distribution systems," in *Proc. 2016 IEEE Int. Telecommun. Energy Conf.*, Austin, TX, USA, 2016, pp. 1–8.
- [10] J. Liu, K. W. E. Cheng, and J. Zeng, "A unified phase-shift modulation for optimized synchronization of parallel resonant inverters in high frequency power system," *IEEE Trans. Ind. Electron.*, vol. 61, no. 7, pp. 3232–3247, Jul. 2014.
- [11] P. T. Sivasubramanian, S. K. Mazumder, H. Soni, A. Gupta, and N. Kumar, "A dc/dc modular current-source differential-mode inverter," *IEEE J. Emerg. Sel. Topics Power Electron.*, vol. 4, no. 2, pp. 489–503, Jun. 2016.
- [12] W. Guo and P. K. Jain, "A power-factor-corrected ac-ac inverter topology using a unified controller for high-frequency power distribution architecture," *IEEE Trans. Ind. Electron.*, vol. 51, no. 4, pp. 874–883, Aug. 2004.
- [13] A. Deutsch *et al.*, "When are transmission-line effects important for on-chip interconnections," in *Proc. Electron. Compon. Technol. Conf.*, 1997, pp. 704–712.
- [14] V. Dzhankhotov, J. Pyrhonen, P. Silventoinen, M. Kuisma, and T. A. Minav, "A new passive hybrid air-core foil filter for modern power drives," *IEEE Trans. Ind. Electron.*, vol. 58, no. 5, pp. 1757–1762, May 2011.
- [15] K. K. F. Yuen and H. S. H. Chung, "A low-loss "RL-plus-C" filter for overvoltage suppression in inverter-fed drive system with long motor cable," *IEEE Trans. Power Electron.*, vol. 30, no. 4, pp. 2167–2181, Apr. 2015.
- [16] Y. Jiang, W. Wu, Y. He, H. S. H. Chung, and F. Blaabjerg, "New passive filter design method for overvoltage suppression and bearing currents mitigation in a long cable based PWM inverter-fed motor drive system," *IEEE Trans. Power Electron.*, vol. 32, no. 10, pp. 7882–7893, Oct. 2017.
- [17] X. Chen, D. Xu, F. Liu, and J. Zhang, "A novel inverter-output passive filter for reducing both differential- and common-mode dv/dt at the motor terminals in PWM drive systems," *IEEE Trans. Ind. Electron.*, vol. 54, no. 1, pp. 419–426, Feb. 2007.
- [18] M. J. Melfi, "Low-voltage PWM inverter-fed motor insulation issues," *IEEE Trans. Ind. Appl.*, vol. 42, no. 1, pp. 128–133, Jan.–Feb. 2006.

- [19] G. Kan, S. Huang, and X. Zou, "Active damping of output LCL filter in PWM inverter-fed drive system with long motor cable," in *Proc. Int. Conf. Elect. Mach. Syst.*, 2016, pp. 1–4.
- [20] A. F. Moreira, P. M. Santos, T. A. Lipo, and G. Venkataramanan, "Filter networks for long cable drives and their influence on motor voltage distribution and common-mode currents," *IEEE Trans. Ind. Electron.*, vol. 52, no. 2, pp. 515–522, Apr. 2005.
- [21] K. Hatua, A. K. Jain, D. Banerjee, and V. T. Ranganathan, "Active damping of output LC filter resonance for vector-controlled VSI-fed ac motor drives," *IEEE Trans. Ind. Electron.*, vol. 59, no. 1, pp. 334–342, Jan. 2012.
- [22] M. A. Mannah, N. Ginot, and C. Batard, "Effect of the power cable on data transmission over a pulse-width-modulated network," *IEEE Trans. Ind. Electron.*, vol. 61, no. 8, pp. 4238–4245, Aug. 2014.
- [23] P. K. Sood and T. A. Lipo, "Power conversion distribution system using a high-frequency ac link," *IEEE Trans. Ind. Appl.*, vol. 24, no. 2, pp. 288–300, Mar./Apr. 1988.
- [24] T. Mishima, S. Sakamoto, and C. Ide, "ZVS phase-shift PWM-controlled single-stage boost full-bridge ac-ac converter for high-frequency induction heating applications," *IEEE Trans. Ind. Electron.*, vol. 64, no. 3, pp. 2054–2061, Mar. 2017.
- [25] S. Jain and V. Sonti, "A highly efficient and reliable inverter configuration based cascaded multilevel inverter for PV systems," *IEEE Trans. Ind. Electron.*, vol. 64, no. 4, pp. 2865–2875, Apr. 2017.
- [26] S. S. Lee and Y. E. Heng, "Improved single-phase split-source inverter with hybrid quasi-sinusoidal and constant PWM," *IEEE Trans. Ind. Electron.*, vol. 64, no. 3, pp. 2024–2031, Mar. 2017.
- [27] A. Gupta, N. Kumar, and S. K. Mazumder, "Frequency-dependent criterion for mitigation of transmission line effects in high frequency distributed power systems," in *Proc. IEEE Energy Convers. Congr. Expo.*, 2015, pp. 4624–4631.
- [28] C. Li and K. Xiaole, "Effects of ground vias on high-speed signal transmission in high-speed PCB design," in *Proc. IEEE Electron. Packag. Technol. High Density Packag.*, 2010, pp. 88–91.
- [29] A. Deutsch *et al.*, "High-speed signal propagation on lossy transmission lines," *IBM J. Res. Develop.*, vol. 34, no. 4, pp. 601–615, 1990.
- [30] I. Takahashi and G. J. Su, "A 500 Hz power system-power converter and transmission lines," in *Conf. Rec. IEEE Ind. Appl. Soc. Annu. Meeting*, 1989, pp. 988–995.
- [31] T. Nakamura, G. J. Su, and I. Takahashi, "A 500 Hz power system—Microprocessor control of the power converter," in *Proc. Rec. KANSAI-Sec. Joint Conv. IEEE*, Japan, vol. 1, 1988, pp. 988–995.
- [32] J. M. Correa, S. Chakraborty, M. G. Simoes, and F. A. Farret, "A single phase high frequency ac microgrid with a unified power quality conditioner," in *Proc. 38th IAS Annu. Meeting Conf. Rec. Ind. Appl. Conf.*, 2003, vol. 2, pp. 956–962.
- [33] H. Ohguchi, M. H. Ohsato, T. Shimizu, G. Kimura, and H. Takagi, "A high-frequency electronic ballast for HID lamps based on a $\lambda/4$ -long distributed constant line," *IEEE Trans. Power Electron.*, vol. 13, no. 6, pp. 1023–1029, Nov. 1998.
- [34] S. Sander, "Buck and boost converters with transmission lines," *IEEE Trans. Power Electron.*, vol. 27, no. 9, pp. 4013–4020, Sep. 2012.
- [35] T. Kawahara, T. Shimizu, M. Shioya, and G. Kimura, "High frequency power transmission by lumped constant circuit replaced distributed constant line," in *Proc. 15th Annu. Conf. IEEE Ind. Electron. Soc.*, 1989, pp. 77–81.
- [36] S. Suzuki and T. Shimizu, "A high-frequency current-output-type inverter aimed for wireless power transmission system," in *Proc. IEEE Energy Convers. Congr. Expo.*, 2015, pp. 5732–5740.
- [37] S. Sander and A. Karvonen, "Semiconductor component reduction in AC/DC converters with transmission lines," in *Proc. Eur. Conf. Power Electron. Appl.*, 2013, pp. 1–10.
- [38] D. M. Pozar, *Microwave Engineering*. 4th ed. Hoboken, NJ, USA: Wiley, Nov. 2011, p. 728.
- [39] M. Zahn, *Electromagnetic Field Theory: A Problem Solving Approach*. Malabar, FL, USA: Krieger Publishing Company, 2003.



Ankit Gupta (S'11) received the B.E. degree in electrical engineering from Delhi College of Engineering, Delhi, India, in 2011. He is currently working toward the Ph.D. degree in electrical and computer engineering at the University of Illinois at Chicago, Chicago, IL, USA.

From 2011 to 2013, he was an Engineer with the super critical Turbo-Generator manufacturing facility of Bharat Heavy Electrical Ltd, HEEP, Haridwar unit. In 2013, he joined the Laboratory of Energy and Switching Electronics System, University of Illinois, Chicago. His research interests include but not limited to GaN-based high density power converters, high-frequency power transmission, microgrids, and grid integration of renewable energy.

Mr. Gupta is an active member of the IEEE MGA community and in 2015 served as the IEEE Region 4 student representative. He also serves as a reviewer for the IEEE TRANSACTION ON POWER ELECTRONICS and IEEE TRANSACTION ON INDUSTRIAL ELECTRONICS.



Nikhil Kumar (S'15) received the B.E. degree in electrical engineering from Delhi College of Engineering, Delhi, India, in 2011, and the M.S. degree in electrical and computer engineering from the University of Illinois at Chicago (UIC), Chicago, IL, USA, in 2015, where he is currently working toward the Ph.D. degree in electrical and computer engineering. His M.S. thesis project at UIC was on developing frequency-dependent criterion to mitigate effects of transmission line terminated with linear loads.

He was an Executive Engineer with Larsen & Toubro, Mumbai, India, from 2011 to 2013. In 2015, he joined Laboratory of Energy and Switching Electronics Systems, UIC. His research interests includes but are not limited to high-frequency link converters, formulation of network control, dc/dc converters and GaN-based switching power converters.



Sudip K. Mazumder (S'97–M'01–SM'03–F'16) received the M.S. degree in electrical power engineering from Rensselaer Polytechnic Institute, Troy, NY, USA, in 1993, and the Ph.D. degree in electrical and computer engineering from Virginia Tech, Blacksburg, VA, USA, in 2001.

He is a Professor with the University of Illinois at Chicago (UIC), Chicago, IL, USA, and is the President of NextWatt LLC. He has over 25 years of professional experience and has held R&D and design positions in leading industrial organizations and has served as a Technical Consultant for several industries. He has published more than 200 refereed papers, delivered more than 80 invited presentations, and received and carried out about 50 sponsored research since joining UIC.

Prof. Mazumder was the recipient of UIC's Inventor of the Year Award (2014), University of Illinois' University Scholar Award (2013), ONR Young Investigator Award (2005), NSF CAREER Award (2003), and IEEE Power Electronics Society (PELS) Transaction Paper Award (2002). He has served on several prestigious NSF panels. In 2016, he was elected to serve as a Distinguished Lecturer for the IEEE PELS beginning in 2016. He has served/is serving as the Guest Editor-in-Chief/Editor for the IEEE PELS/IES Transactions between 2013 and 2017, as the first Editor-in-Chief for Advances in Power Electronics (2006–2009), and as an Editorial Board Member for the IEEE IES/PELS/TII/JESTPE/TAES Transactions. He currently serves as the Chair for the IEEE PELS TC on Sustainable Energy Systems.